Strategies for successful realization of strong confinement microphotonic devices.

Tymon Barwicz*, Milos A. Popovic, Michael R. Watts, Peter T. Rakich, Charles W. Holzwarth, Franz X. Kaertner, Erich P. Ippen, and Henry I. Smith.
Research Laboratory of Electronics, Massachusetts Institute of Technology, Cambridge MA, USA
*Current address: IBM T.J. Watson Research Center, Yorktown Heights NY, USA

ABSTRACT

Microphotonic devices employing strong confinement of light are of growing importance for key applications such as telecommunication and optical interconnects. They have unique and desirable characteristics but their extreme sensitivity to dimensional variations makes them difficult to successfully implement. Here, we discuss strategies towards the successful realization of strong confinement devices. We leverage what planar fabrication technology does best: replicating structures. Although the absolute dimensional control required for successful fabrication of many strong confinement devices is all but impossible to achieve, we show that surprisingly-high relative dimensional accuracy can be obtained on structures in proximity of one another on a wafer. This provides an advantage to schemes that are based on multiple copies of low-complexity structures. These copies can be made nearly identical or with precise relative-dimensional offsets to achieve the desired function. We quantify the achievable relative dimensional control and discuss the first demonstration of multistage filters, integrated polarization diversity, and high-order microring-filter banks.

Keywords: Microphotonics, add-drop filter, microring resonator, microfabrication, resonance frequency.

1. INTRODUCTION

Microphotonic devices employing strong confinement of light, such as photonic crystals and micron-sized resonators, have unique and desirable characteristics. However, their extreme sensitivity to dimensional variations makes them difficult to successfully implement. In this paper, we discuss strategies towards the successful realization of strong confinement devices. Mainly, we leverage what planar fabrication technology does best: replicating structures. Although the absolute dimensional control required for successful fabrication of many strong confinement devices is all but impossible to achieve, we show that it is possible to fabricate nearly identical structures in proximity of one another on a wafer. Moreover, it is possible to induce, in these structures, precise and accurate relative dimensional offsets. The absolute dimensions of those structures will likely be biased by at least a couple of nanometers from the intended design. However, this bias can be made nearly identical, within tens of picometers, for all the structures of interest. This enables the successful implementation, even without post-fabrication trimming, of strategies relying on multiple copies of identical structures to achieve the desired operation. Below, we quantify the achievable relative dimensional control on nearby structures. We achieve a ~25 pm measurement precision on the relative dimensional control on the average dimensions of microring resonators of a filter. Such dimensional sensitivity is provided by the exceptional sensitivity of some filter responses to frequency mismatch of the resonators forming the filter. Then, we present high performance devices based on schemes relying on the strict relative dimensional control on nearby structures. These schemes include multistage microring filters, integrated polarization diversity, and high-order microring-filter banks.

2. FABRICATION CONTROL

Variations in properties of fabricated photonic structures mainly originate from two distinct sources: (1) in-plane dimensional variations due to lithographic imperfections; (2) variations of the thickness and optical properties of the high-index thin-film serving as the index-guiding layer for the photonic structures. Dramatic wafer-to-wafer variations in the properties of strong confinement photonic structures can be observed. Nonetheless, these variations are dramatically reduced when comparing structures in close proximity to one another on a given wafer.

The optical properties and the thickness of a thin film can vary significantly on a wafer and from one wafer to another. However, these variations become negligible on the sub-millimeter scale. Correspondingly, the absolute dimensional

Silicon Photonics III, edited by Joel A. Kubby, Graham T. Reed
Proc. of SPIE Vol. 6898, 68980N, (2008) · 0277-786X/08/$18 · doi: 10.1117/12.765986

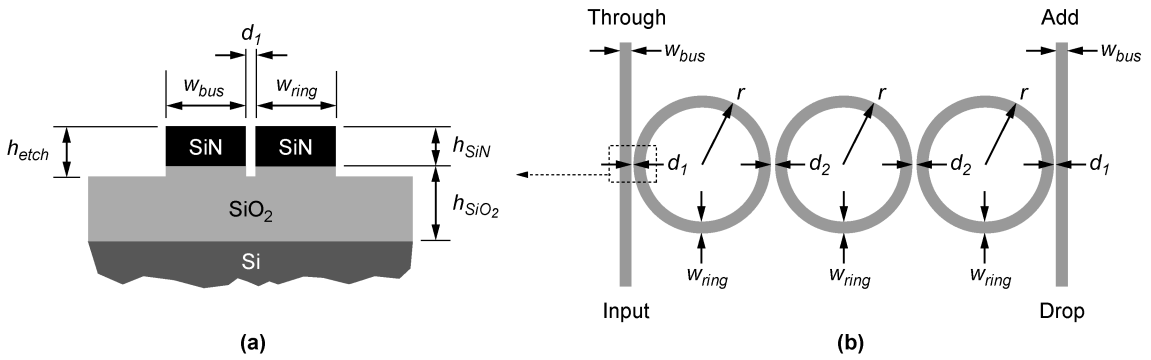

Fig. 1 Schematic of the series-coupled third-order microring filters used. The microrings are designed to be alike and the parameters are shown in Table I. (a) Cross-section of the waveguides at the bus-to-ring coupling region. (b) Top view.

Table 1 Designed filter parameters

Parameter	Filters with symmetric coupler design.	Filters with asymmetric coupler design.
h_{SiN}	400 nm	396 nm
h_{SiO2}	3 µm	3 µm
h_{etch}	500 nm	600 nm
n_{SiN}	2.200	2.181
n_{SiO2}	1.455	1.455
w_{bus}	804 nm	702 nm
w_{ring}	804 nm	900 nm
d_1	102 nm	120 nm
d_2	492 nm	372 nm
r	8004 nm	7998 nm

All lithographically defined dimensions were rounded to a 6 nm scanning-electron-beam-lithography step-size to ensure consistent discretization of patterns.

control (expected wafer-to-wafer dimensional variation) at fabrication is usually on the order of +/- 5 nm. However, the relative dimensional control of structures in proximity of one another on a given wafer can be orders of magnitude better.

To achieve high relative dimensional control on structures in proximity of one another, the key is to understand the source of errors in the lithographic system used and layout the devices correspondingly to remove any systematic error components. In most cases, the main sources of lithographic errors on structures in proximity of one another are proximity effects and lithographic field distortion. If a vector-scan electron-beam lithography system is used, differences in the employed writing strategy can also have a significant impact. Proximity correction algorithms usually only provide a first-order correction, which is insufficient for most microphotonic devices. To minimize variations, key photonic structures should have similar lithographic surroundings. Moreover, if a scanning electron-beam lithography system (SEBL) is used, the key structures should be placed at the same intra-field position within their corresponding writing fields and have the same orientation. This will ensure that systematic errors due to intra-field distortions and differences in writing strategies are minimized. If an optical lithography system is used, the situation is a little more complicated as lithographic imperfections on the SEBL written mask are convoluted with the imperfections of the optical system. For the rest of this paper, we focus on structures directly written by SEBL.

To study the fabrication control of structures in close proximity to one another we have used third-order series-coupled microring-resonator filters with silicon-rich silicon nitride waveguide cores. Two designs were employed and are described in Fig. 1 and Table 1. The second design used an asymmetric coupling region to prevent coupling of the

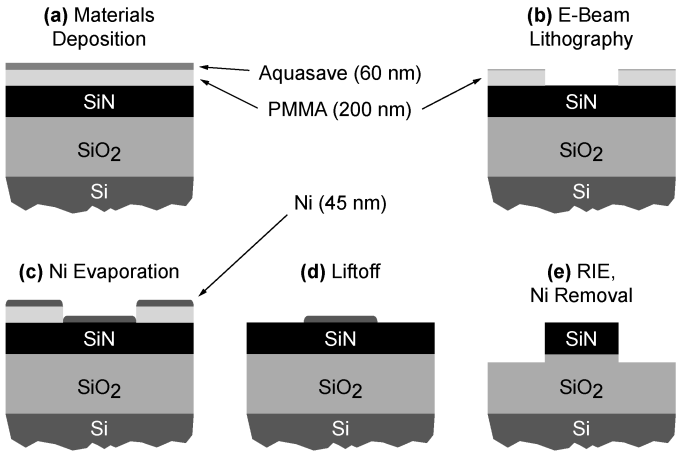

Fig. 2 Fabrication process overview. The initial multilayer is formed of 3 um of silicon oxide, 400 nm of silicon-rich silicon-nitride (SiN), 200 nm of poly-methyl-methacrylate (PMMA) and 60 nm of Aquasave.[2]

fundamental resonant mode to a spurious higher-order mode allowed in the coupling region of the asymmetric coupler design. This coupling resulted in significant coupler loss for the first design and was solved with the asymmetric coupler design.[1]

The filters were fabricated with the fabrication process shown in Fig.2. First, a Si wafer was thermally oxidized to form a 3-um-layer of SiO_2. Then, a 400-nm-thick SiN layer was deposited by low-pressure chemical-vapor-deposition (LPCVD) in a vertical thermal reactor with a gas mixture of SiH_2Cl_2 and NH_3. The resulting SiN shows low stress and is often referred to as low-stress nitride. Next, 200 nm of poly-methyl-methacrylate (PMMA) and 60 nm of Aquasave were spun on. PMMA is a positive e-beam resist while Aquasave [2] is a water-soluble conductive polymer used to prevent charging during SEBL. The PMMA was exposed at 30 KeV using a Raith 150 SEBL system. The Aquasave was removed, and the PMMA developed. Next, 45 nm of Ni was evaporated on the structure, and a liftoff performed by removing the non-exposed PMMA. Using the Ni as a hardmask, the waveguides were defined by conventional reactive-ion-etching (RIE) with a gas mixture of CHF_3-O_2. To obtain an accurate etch depth, the RIE is performed in several steps, between which the etch depth is measured with a profilometer. Finally, the Ni was removed using a nitric-acid-based commercial wet Ni etchant and the sample prepared for optical characterization. Fabricated filters are shown in Fig.3.

The through-port response of a third-order series coupled microring filter is surprisingly sensitive to any frequency mismatch between the resonators forming the filter and, in particular, to a frequency mismatch between the inner and the outer microrings. Thus, any difference in frequency between the microrings forming the filter can be accurately deducted from the filter response. From this frequency mismatch, the dimensional difference between the microrings can be obtained.

Fig. 3 Electron micrographs of fabricated filters with (a) symmetric coupler design and (b) with asymmetric coupler design.

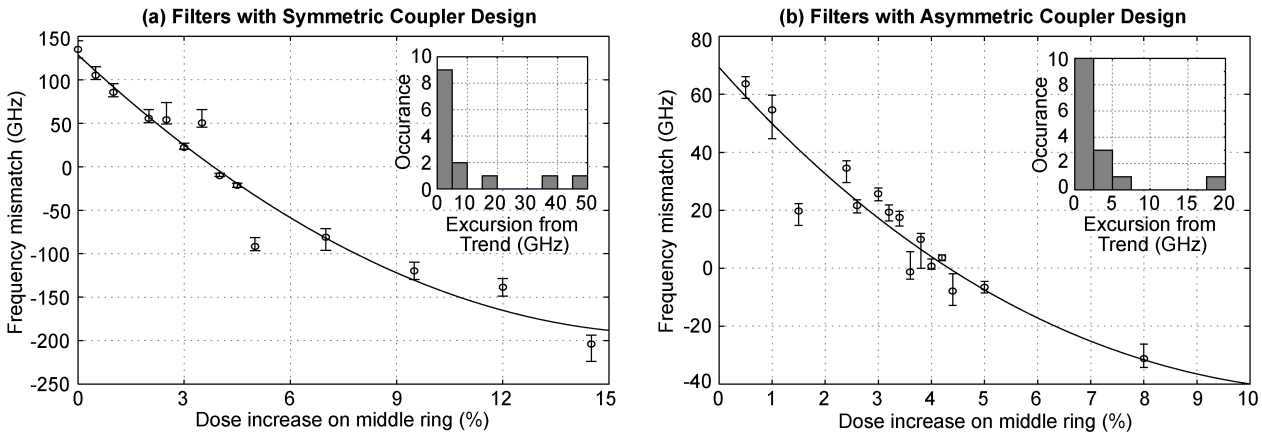

Fig. 4 Empirical relationships between frequency mismatch and dose increase on middle ring in filters with (a) symmetric coupler design and (b) asymmetric coupler design. Parabolic trend lines were introduced in the graphs. The insets show the data point to trend line excursions that cannot be explained by measurement and fitting errors. A better controlled fabrication process and wider ring-waveguide widths allowed for a tighter distribution of frequencies in (b).

Figure 4 shows the measured frequency mismatch between inner and outer microrings for two sets of filters corresponding to the two filter designs. On one photonic chip, fourty filters with symmetric coupler design were spaced by 200 um to form an 8 mm wide set. On another photonic chip, thirty filters with asymmetric coupler design were spaced by 400 um to form a 12 mm wide set. On both sets, the SEBL exposure dose of the middle ring was incrementally increased to experimentally measure the impact of the exposure dose on the microring frequency and, in turn, on the microring dimensions. Adjusting the exposure dose at SEBL allows introduction of minute dimensional offsets which can be used to introduce precise and accurate frequency offsets in adjacent resonators. The stochastic variations of the resonance frequency are provided by the offsets of the data points from the trend line and are counted in the insets of Fig.4. From mode-solver analyses, the microring resonance frequency is expected to change by 38 GHz per nanometer of ring-waveguide width for filters with symmetric coupler design and by 29 GHz per nanometer of ring-waveguide width for filters with asymmetric filter design. Using the computed sensitivity and the measured frequency offsets we can say that the observed frequency variations correspond to stochastic variations of the average width of the middle microring of the order of 0.1 nm. This reflects the achievable relative dimensional control on such structures.

The frequency mismatch at zero excess dose on the middle microring is mainly due to SEBL proximity effects and to coupling-induced frequency shifts (CIFS), an effect unrelated to fabrication imperfections. CIFS is a shift of the resonance frequency of a resonator due to refractive-index perturbation created by an adjacent waveguide in a coupling region and is described in Ref. 3. As the bus-to-ring coupling is stronger than the ring-to-ring coupling, an effective frequency mismatch appears between the inner and the outer microrings. This difference in coupling is realized in practice by a difference in the coupling gaps, which, in turn, creates a different lithographic environment for the inner and outer microrings and results in an additional frequency mismatch due to proximity effects. A calculation of the variation in the inner and outer radii along an inner and an outer microrings are shown in Fig.5. The details of the calculation are presented in Ref. 4. Fig. 5 shows the clearing-dose contours plotted for various SEBL doses, expressed as relative offsets from a reference dose chosen as the SEBL area dose minimizing the width variations in all microrings. The shape of the microrings and all relative dimensions follow approximately the contours of constant dose corresponding to the clearing dose of the e-beam resist. However, the absolute dimensions of the microrings will be consistently offset from these contours by the fabrication process. The microring shape is a function of the SEBL area dose used, which is illustrated in Fig. 5. As expected, the ring waveguides are wider for higher e-beam doses. The largest ring-waveguide widths are obtained near the small bus-to-ring coupling gaps while the smallest ring-waveguide widths are obtained near the top and bottom of the middle rings [in orientation of Fig. 5(a)]. The dose profile of each filter has two axes of symmetry (one vertical and one horizontal) going through the center of the middle ring of the filter. When the same dose is used on middle and outer rings, the width of the middle ring is smaller than the width of the outer rings. Moreover, as the outer and inner radii are differently affected by proximity effects, the ring circumference will be larger in the outer rings than in the middle ring. These raise the resonant frequency of the middle ring and create a

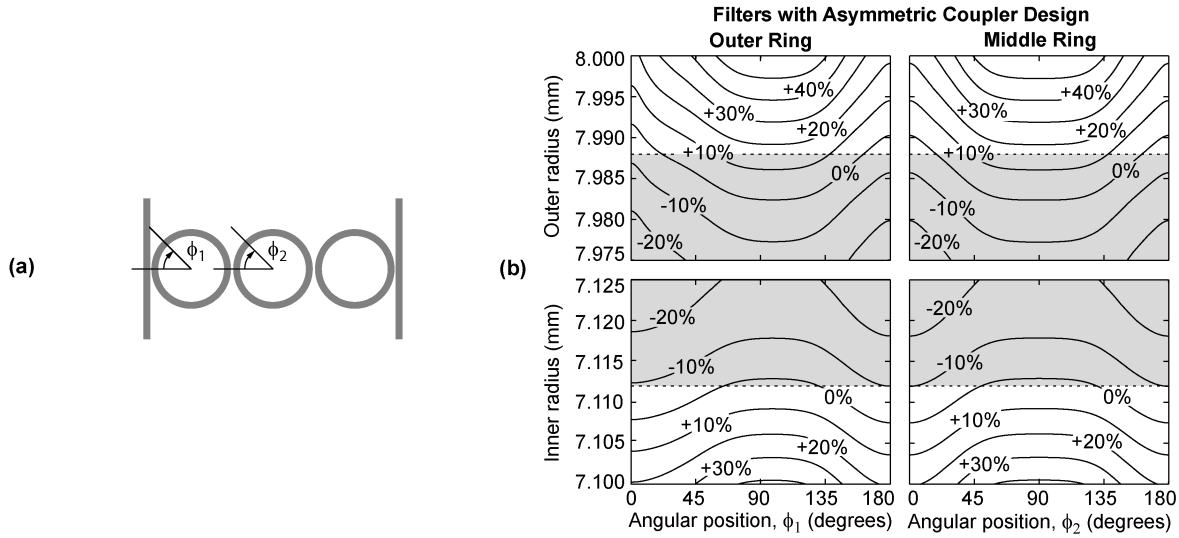

Fig. 5 Resist clearing-dose contours for various SEBL area doses expressed as relative offsets from the dose minimizing the width variations in all ring-waveguides of a filter. The ring-waveguide edges will follow the clearing dose contours but will be consistently offset by the fabrication process. (a) Definition of angular positions along the outer and middle rings. (b) Clearing-dose contours for filters with asymmetric coupler design. The dotted lines represent the positions of the ring-waveguide edges in the SEBL layout and take into account the width bias used in fabrication. The shaded areas correspond to regions exposed by the SEBL.

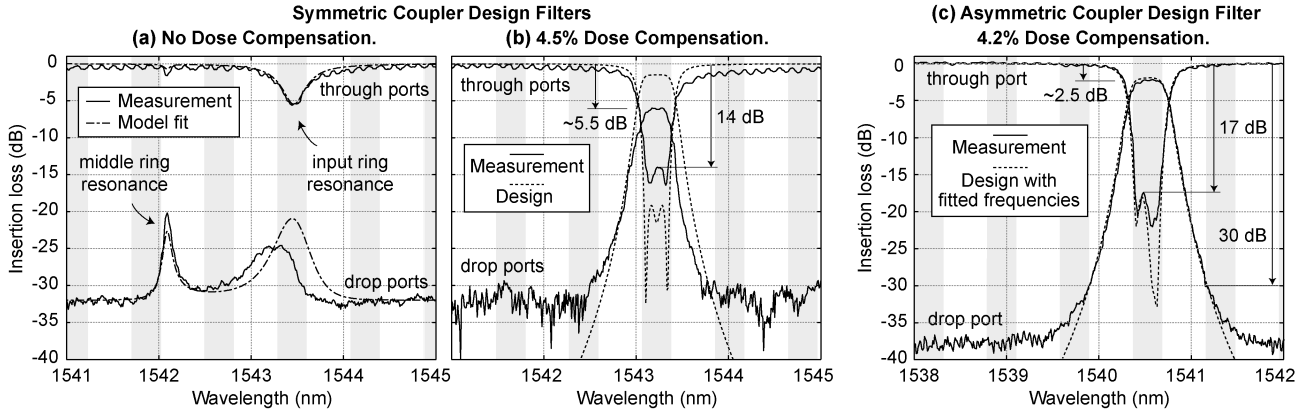

Fig. 6 Spectral responses of filters with symmetric coupler design with (b) and without (a) excess SEBL dose on the middle microring. (c) Spectral response of a filter with asymmetric coupler design and excess dose on the middle microring. The resonant frequencies of the microrings of the filters reported in (b) and (c) are matched to better than 1 and 2 GHz, respectively.. The ACD improved the filter drop loss by reducing coupler scattering, a significant source of loss identified in our previous work.[1]

frequency mismatch with the outer rings. This frequency mismatch is a function of the global SEBL area dose used as the shapes of the middle and outer rings are differently affected by a dose change.

The incremental excess dose applied to the middle microring in the experiment of Fig. 4 lowers the resonance frequency of that microring. However, this dose increase will also lower the resonant frequency of the outer rings through proximity effects. This phenomenon was computationally estimated. For a given dose compensation, it was found that

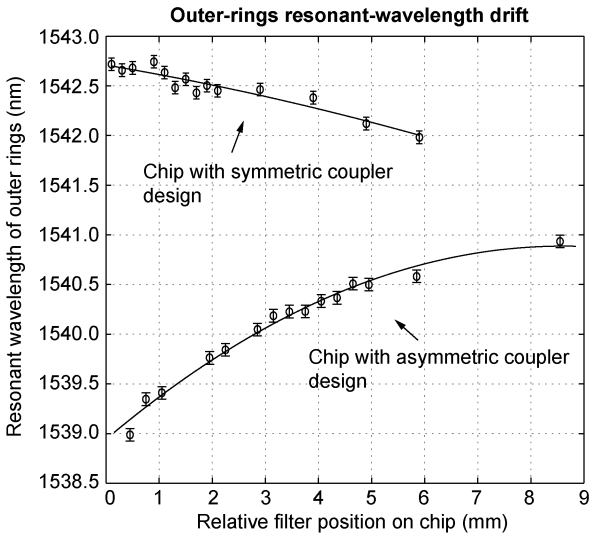

Fig. 7 Absolute resonant frequency of outer rings with relative filter position. The frequency drift is most probably dominated by variations of the SiN thickness with filter position.

the outer rings' resonant frequency will be decreased by 3.0%–3.5% of the decrease of the middle ring resonant frequency. Thus, this secondary effect can be mostly neglected.

Figure. 6 shows the spectral response of the uncompensated and best compensated filters to illustrate the data acquisition and the fitting performed. The best compensated filters show a 1 and a 2 GHz mismatch, respectively. This frequency matching indicates that the average ring-waveguide-widths are within 26 and 68 pm, respectively, of the needed dimensional offsets for perfect compensation of the frequency mismatch at zero excess dose on the middle microring.

As the above sets of filters extend to a few millimiters, it is also possible to observe frequency drifts due to longer scale variations as well. For this purpose, the resonance frequency of the outer microrings of a filter in function of the filter position is plotted in Fig. 7. The form of the resonance-drift points toward variation of the SiN thickness as the cause of the drift. In fact, the resonance frequency shows a sensitivity of 70 GHz per nanometer of SiN thickness. Such thickness non-uniformity is particularly problematic in bonded silicon-on-insulator wafers with thick buried oxide, which is the key wafer type for most silicon photonics.

3. MULTISTAGE FILTERS

Multistage filters are a good example of structures taking advantage of the high relative dimensional control on sub-millimeter-spaced structures demonstrated above. Multistage filters are high-order add–drop filters constructed by incoherently cascading reduced-order stages.[5] The resulting through-port responses are shown to be less sensitive to errors in coupling coefficients and resonance frequencies. These errors make it difficult to achieve high through-port extinction in a single, high-order, series-coupled filter. In addition, multistage filters permit lower drop loss because of the partial decoupling of the drop- and through-port synthesis. However, for the multistage approach to be preferred, the multiple stages of a multistage filter need to be fabricated with great uniformity from one stage to the next. Thus, relative dimensional control on structures in close proximity to one another is critical in this approach.

In Fig. 8, we illustrate theoretically the filter response sensitivity for a fourth-order filter that meets typical criteria for a 100 GHz spaced WDM channel grid with a multistage filter meeting comparable requirements. We incorporated finite cavity loss Q's of 25,000. Fig. 8 shows 1000 overlaid responses representing a uniformly distributed random fractional error in power couplings and in frequency mismatch as a fraction of bandwidth (±15% in both cases). For the fourth-order filter, the extinction is limited by the random perturbations to ~10 dB. By comparison, in a multistage filter formed of three cascaded third-order stages, the resulting drop loss is lower (here, 2.5 dB instead of 3 dB) and a more robust

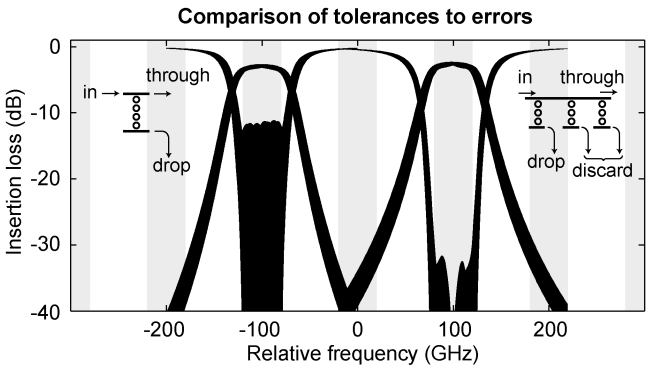

Fig. 8 Loss and tolerance to errors of comparable single-stage (left) and multistage (right) filters.

total through-port extinction of 30 dB is achieved. Moreover, if comparing filters of even higher-order than illustrated here, multistage designs provide with even greater drop loss reduction.

Multistage filters were fabricated by incoherently cascading the filters with asymmetric coupler design discussed above. The exposure pattern was designed for lithographic field distortions to affect the filter stages in common mode such that each stage remains frequency aligned with the other ones. To achieve frequency matching of all resonators of the filter, a 3.8%–4.2% higher electron-beam dose was applied to the middle ring of each stage to precisely increase its dimensions and match its resonance frequency to the outer rings. Fig. 9(a) shows a scanning electron micrograph of a fabricated three-stage device.

Figure 9(b)–9(d) show measured drop- and through-port transverse-electric (TE) responses of one-, two-, and three stage filters. Close agreement between the intended design and the measured result for a single-stage filter [Fig. 9(b)] validates the design and demonstrates the fabrication accuracy. The only fitted parameters were the center wavelength of 1538.36 nm and the middle-to-outer ring resonance frequency mismatch of 2.3 GHz. Excess ring propagation loss of 12 dB/cm

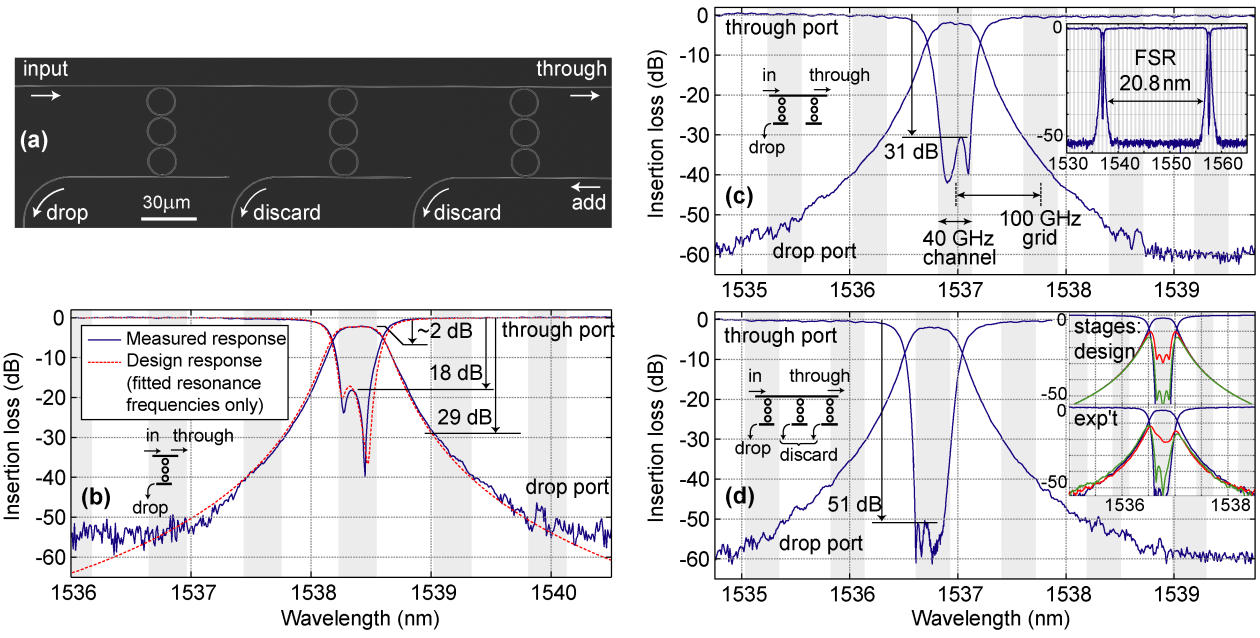

Fig. 9 (a) SEM of fabricated three-stage filter. Measured response spectra of (b) one- (with design plot), (c) two- (inset shows FSR), and (d) three-stage filter showing high in-band extinction (inset, individual stage responses).

was extracted by independent measurement and included in the model. The single-stage filter has a 40 GHz 1 dB passband with 2 dB drop loss, 30 dB out-of-band rejection, and 18 dB through-port extinction. This is the highest reported extinction in a high-order microring filter to our knowledge. The excellent extinction is mainly attributed to the frequency matching and low loss. The dispersion is zero near the center band with an average slope of ~0.3 ns/nm^2. The two-stage filter [Fig. 9(c)] shows a similar drop response with increased through-port extinction of over 30 dB across the channel. This meets typical requirements for WDM add–drop filtering. The inset shows a realized FSR above 20 nm. In three-stage filters, the observed extinction [Fig. 9(d)] is above 51 dB across a 32 GHz window and was found to be limited by frequency mismatch. Microrings in filters with appropriate dose compensation on the center microring are synchronous to ~2 GHz. This corresponds to a matching of average ring widths to better than 68 pm. The three-ring filter stages are frequency aligned to ~5 GHz [Fig. 9(d) inset]. The excellent stage alignment is a critical requirement for practicability of multistage filters without post-fabrication or active adjustment of individual rings. Adjacent channel insertion loss in the through port of a single stage is <0.3 dB, which can limit the tolerable number of stages. These multistage add–drop filters demonstrated the first high-extinction, rectangular notch spectra achieved in microring resonators. These were also the first microphotonic filters to show low-loss, high-fidelity flattop responses that meet the full spectral requirements of WDM add–drop filtering.

4. POLARIZATION TRANSPARENCY

Integrated polarization diversity is another example of a scheme relying on the high relative dimensional control on sub-millimeter-spaced structures. It is all but impossible to fabricate strong-confinement devices with the required accuracy for polarization-transparent operation. However, as discussed below, it is possible to use two identical copies of polarization-sensitive photonic structures with appropriately arranged polarization splitters and rotators to achieve polarization transparent operation. This scheme relies on achieving two optically-identical copies of structures and has been highly successful experimentally. Almost complete elimination of polarization sensitivity is shown.

Polarization-transparent devices can be constructed from polarization-sensitive components using the integrated polarization diversity scheme shown in Fig. 10. The arbitrary polarization state emanating from a fiber is split into orthogonally polarized components traveling in separate arms. By rotating the polarization state in one of these arms, a single polarization is realized on-chip. The two arms then pass through identical sets of polarization-sensitive photonic structures. At the output of the chip, another polarization rotation is performed and the two arms are recombined. The second polarization rotation is carried out to avoid wave interference between the two arms. The rotators are placed on opposite arms to achieve overall symmetry, which is key for polarization transparent in the event of imperfect polarization splitters or rotators. In Fig. 10, the photonic structures depicted operate on the TE polarization state, corresponding to an in-plane orientation of the electric field. By rearranging the polarization rotators in the circuit, it is straightforward to construct a polarization diversity scheme for photonic structures operating on the transverse-magnetic (TM) polarization state.

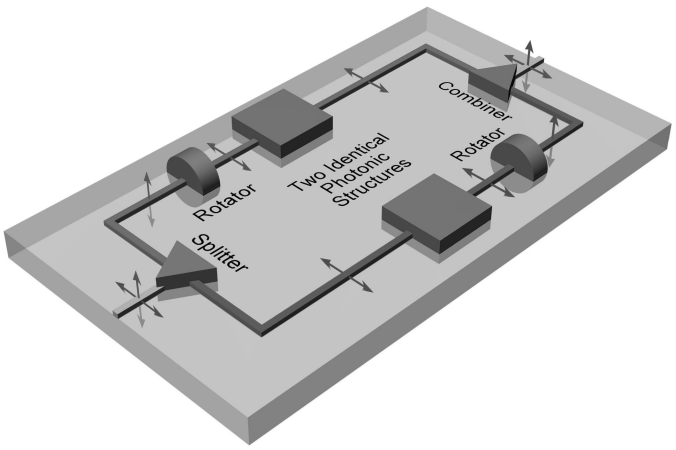

Fig. 10 Integrated polarization diversity scheme. Polarization-transparent microphotonic circuits are constructed from polarization-sensitive components. Arrows depict the orientation of the electric field.

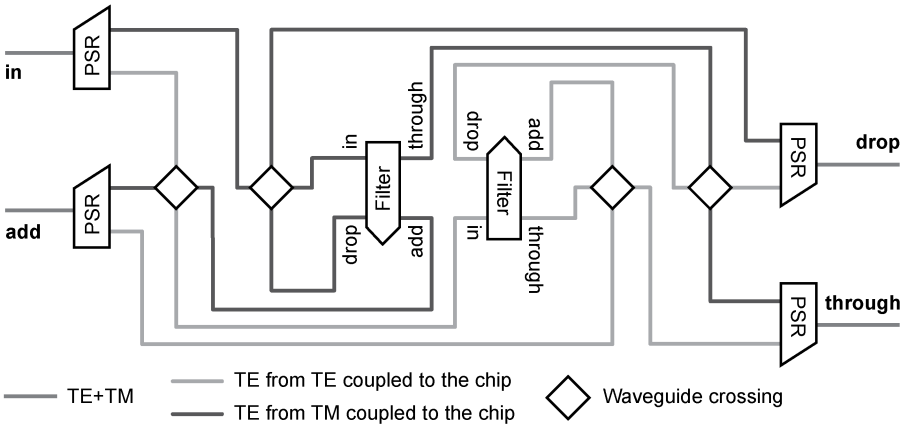

Fig. 11 Functional diagram of the polarization-transparent optical add-drop filter. PSR stands for the polarization splitter and rotator shown in Fig. 12.

To demonstrate the integrated polarization diversity scheme, we have a fabricated a polarization-transparent add-drop filter based on the multistage filters discussed above. A schematic of the polarization-transparent device is presented in Fig. 11. Light of unknown polarization is coupled to the chip from a fiber. First, it reaches a polarization splitter and rotator (PSR), where the light is split into its TE and TM polarization eigenstates, and the TM component is subsequently rotated to become TE. The two components are then directed towards two identical multistage filters. Finally, the light passes through another PSR before exiting the chip towards a fiber. This second PSR is traversed in the reverse direction so that the thus-far non-rotated TE polarized light is rotated to become TM and combined with the other light component. This system is two-fold symmetric and the inputs may be used as outputs.

The PSRs used are shown in Fig. 12. They were designed [6-7] so that it is energetically favorable for the vertically polarized light (TM mode) to tunnel across the narrow gap into the tall waveguide, but the horizontally polarized light (TE mode) remains in the flat waveguide. The TM polarization state is then rotated to become TE by slowly transforming the tall waveguide into a flat one through a structure that emulates a twisting waveguide and mimics the chirality naturally exhibited by large molecules found in nature. The transformations in the PSR are remarkably effective and adiabatic: no coupling between the various modes of the structure is desired. These PSRs have negligible intrinsic

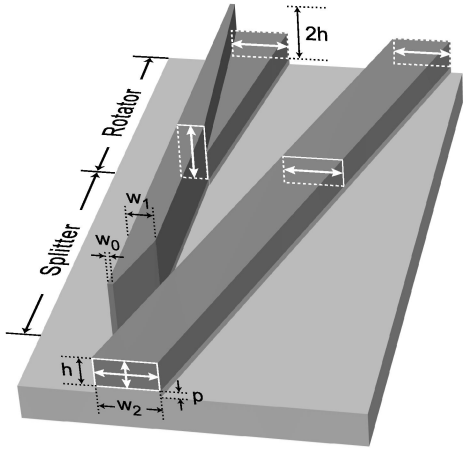

Fig. 12 Schematic of the polarization splitter and rotator (PSR) employed. The white arrows depict the orientation of the electric field in the guides. The values of the parameters are w_0 = 70 nm, w_1 = 360 nm, w_2 = 800 nm, p = 100 nm, and h = 420 nm. The PSR is about 600-um-long The left waveguide is separated from the right waveguide by 200 nm at the onset of the splitter. This separation grows to a micron before the onset of the rotator.

loss and allow a 300-nm bandwidth of polarization-transparent operation.

The waveguide crossings were formed from waveguides that widen adiabatically from 600-nm-wide at the edges of the crossings to 3-um-wide near the center to suppress undesirable crosstalk and loss. The waveguide crossings were designed with three-dimensional finite-difference time domain simulations. Each waveguide was expanded adiabatically until the field of the fundamental mode at the waveguide edges was negligible and the large lateral extent of the mode guaranteed slow diffraction.

Three cascaded third order filters were used for each polarization. The two multistage filters were spaced by 400 um on the chip and their design was similar to the multistage filters discussed above. The optical performance of the fabricated polarization-transparent add-drop filter is presented in Fig. 13 for 40 randomly chosen polarization states at every wavelength. In addition, independently acquired responses of the two polarization eigenstates are overlaid in bold. A low polarization-dependent loss (PDL) with a mean of 1.0 dB and a standard deviation across the spectrum of 0.45 dB is achieved. Of this PDL, 0.3 dB is due to the optical characterization scheme. The optical characterization was perfomed with point-by-point laser transmission measurements. Specific polarization states were generated with a tunable laser and an electronic polarization controller and were coupled into and out of the waveguides with lensed fibers. The chip did not use high-efficiency fiber-to-chip couplers, but the waveguide cross-section at the chip facets was designed to offer polarization transparent coupling efficiency. The TE and TM eigenstates were reliably identified through extinction of the TE and TM resonances of stand-alone ring resonators on the optical chip. The collected laser line was spectrally filtered with a synchronously tuned monochromator (to reject amplified spontaneous emission in the laser) and detected with an InGaAs PIN photodiode through lock-in detection.

The measured polarization-transparent bandwidth exceeds 60 nm. In Fig. 13, the PDL is the vertical distance between the two bold curves. Without the polarization diversity scheme, the underlying microrings would show a spectral misalignment of several nanometres between the responses of the two polarization eigenstates. Here, the spectral misalignment is negligible and corresponds to slight differences in resonant frequency between the two, nominally identical, multistage microring filters in the polarization transparent add-drop filter. As discussed above, the resonant frequencies are controlled at fabrication through the average ring-waveguide width of each microring. Precise adjustments of the e-beam exposure dose were applied to the various microrings and a careful placement of each stage in its corresponding e-beam field was performed to avoid frequency errors due to intra-field distortion. The through-port spectral misalignment corresponds to a relative control of the average ring-waveguide widths of all 18 microrings of the polarization transparent filter to 0.15 nm, and the drop-port spectral misalignment corresponds to a relative control of the average ring-waveguide widths of the 6 microrings of the first stages of the two filters to 0.07 nm. This shows, again, the excellent relative dimensional control achievable on nearby structures.

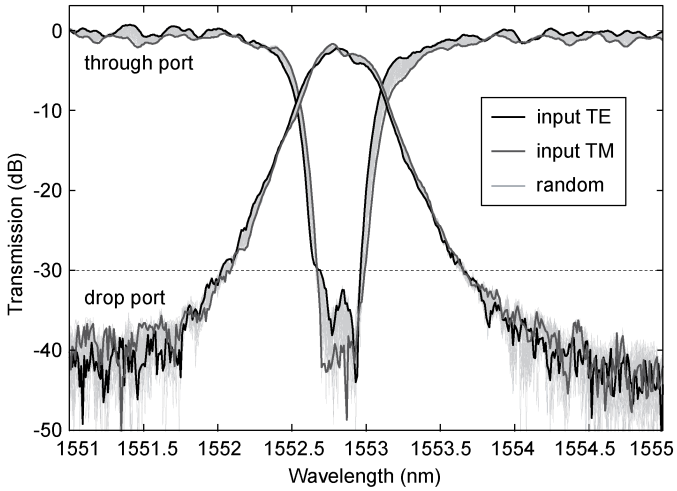

Fig. 13 Spectral response of a fabricated polarization-transparent optical add-drop filter for 40 randomly chosen polarization states at each wavelength. The spectral responses for the two polarization eigenstates are overlaid in bold. The shape of the spectral response below the -30 dB line is of no consequence.

The fabricated polarization-transparent OADF shows a through-port extinction of more than 32 dB and a drop loss of no more than 2 dB. Its bandwidth spans 50 GHz, its free spectral range reaches 2.5 THz (20 nm), and it allows a minimum channel spacing of 130 GHz (1.05 nm). The transmission between the add and the through port is not shown, but is almost identical to the transmission between the input and the drop port. The polarization sensitivity on the bottom of the through-port response is of no consequence as it is below the 30-dB extinction required in OADFs. The spectral oscillations, particularly visible off-resonance in the through-port response, are due to a shortcoming of the scanning electron-beam lithography system that was used and are explained in more detail in the supplementary information associated to Ref. 8.

To our knowledge, the demonstration of integrated polarization diversity was the first successful realization of a strong-confinement microphotonic circuit of such complexity. It is important to note, however, that it is of the minimum complexity required to render completely arbitrary photonic structures polarization transparent.

5. FILTER BANKS

With appropriate empirical calibration, it is possible to create banks of filters with accurate spectral spacing without post-fabrication trimming. The high relative dimensional control on nearby structures can be employed to introduce accurate and precise dimensional offset between the filters for accurate frequency spacing. As previously mentioned, the absolute dimensions are expected to be uniformly offset from the design by at least a couple of nanometers. This will induce a uniform offset in the operating frequency of each filter. However, the frequency spacing will be unaffected. This uniform frequency offset can be remedied by a number of means, one of which is to offset the operating temperature of the photonic chip.

The primary objective was to demonstrate an eight-channel microring-resonator filter bank with accurate channel spacing without post-fabrication trimming for an integrated electronic-photonic analog-to-digital converter, described in Ref. 9. The filters needed to show a free-spectral range of at least 20 nm, a 3 dB bandwidth of 50 GHz, a drop loss of no more than 3 dB, and a passband roll-off sufficiently sharp to limit the crosstalk between 150 GHz-spaced adjacent channels to at least -30 dB. For this purpose, the second-order microring-resonator filters shown in Fig. 14 were designed.

The first step was to empirically calibrate the effect of lithographic parameters on the designed filters. Offsets in e-beam dose were sufficient to achieve the needed relative dimensional offsets for the multistage and polarization transparent filters discussed above. For filter banks, however, the range of the dimensional offsets provided by modification of the e-beam dose without deleterious impact on line-edge roughness was insufficient to achieve the desired 150 GHz spectral spacing. In addition to changes in e-beam dose, offsets in the ring-waveguide inner and outer radii needed to be used as

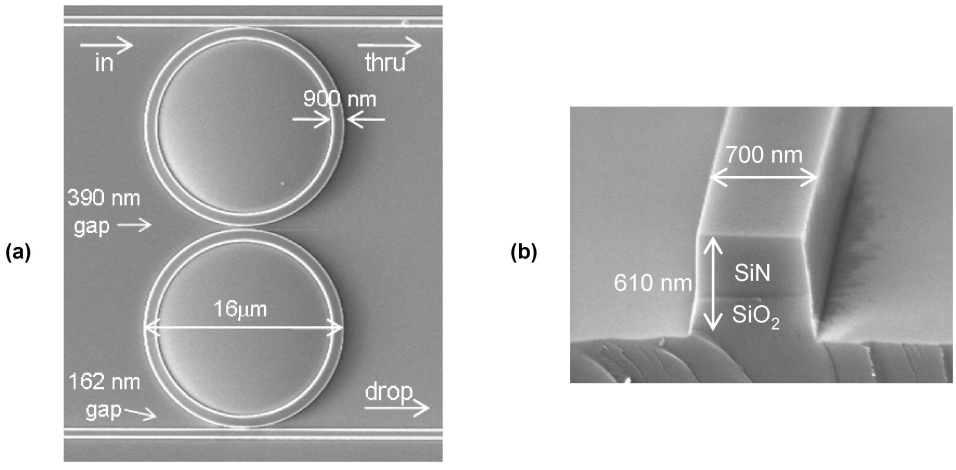

Fig. 14 (a) Scanning-electron micrographs of second-order microring-resonator filter with indicated designed filter dimensions. Actual fabricated dimensions are within 5 nm of the designed dimensions. (b) Cross section view of a bus waveguide etched into 400 nm of SiN and 210 nm of SiO_2.

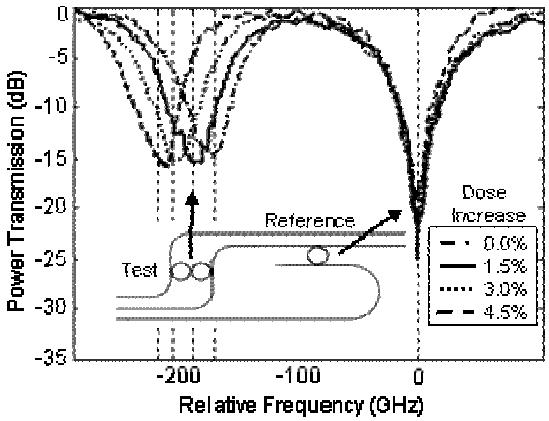

Fig. 15 Sample of transmission spectra used for calibration of the effect of e-beam dose on filter frequency. The insert displays the device layout. A reference filter was used with each test filer. All frequencies were measured relative to the reference filter frequency.

Table 2 Sensitivity of the resonance frequency of a filter to lithographic parameters.

Parameter	Optical Simulations	Calibration	Filter Banks
Radius in e-beam Layout (GHz/nm)	-18.4	-17.2 ± 0.9	-18.0 ± 0.2
Width in e-beam layout (GHz/nm)	-33	-36.6 ± 0.4	NA
Dose (GHz/%)*	-24	-12 ± 2	-11 ± 1

* Frequency shift due to a 1% change in dose

well. Simulations were performed using a two-dimensional cylindrical mode solver to calculate the dependence of the ring's resonance frequency on the inner and outer ring radius and the ring waveguide cross section. These simulations showed that a 1 nm increase in ring radius and waveguide width would produce resonant frequency shifts of −18.4 and −33 GHz, respectively. The discrete 6 nm address grid of the SEBL system, limits the channel spacing possible though changes in the pattern layout to linear combinations of −110 and −198 GHz shifts. To achieve the desired filter bank with channels spaced 150 GHz apart, the resonance frequency was fine-tuned with adjustements of electron-beam dose. An empirical calibration was performed to find the resonant frequency's dependence on specified exposure dose, radius, and width. For this it was important to separate frequency shifts due to changes in lithographic parameters from shifts caused by other factors such as slight changes in the SiN thickness and slow drifts of the electron-beam current. To separate these contributions, each calibration test was performed with a reference filter and a test filter located in close proximity to one another. The reference filter was kept unchanged in all cases while the exposure dose, ring widths, and ring radii were varied on the test filter. The effect of the lithographic alteration on the resonant frequency was determined by measuring the frequency shift of the test filter relative to the resonance frequency of the reference filter. This is shown in Fig. 15.

The resonant frequency dependence on changes in specified exposure dose, ring radius, and ring waveguide width are shown and compared with simulated data in Table 2. The calibration experiments for radius and width changes are close to the simulated values, whereas the frequency dependency on dose was considerably different, reinforcing the need for empirical calibration. Also, during calibration it was shown that frequency shifts due to changes in dose, radius and width add linearly within the range tested.

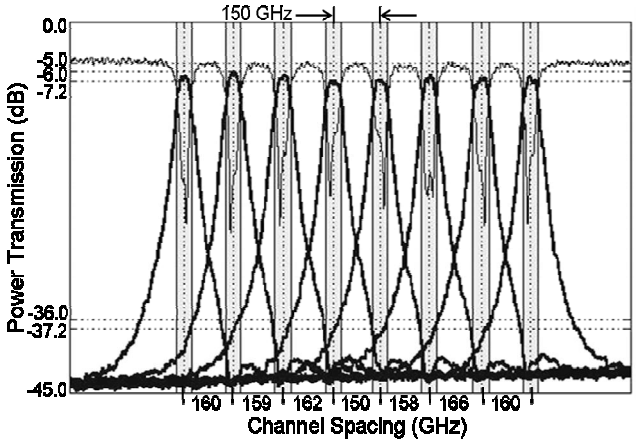

Fig. 16 Measured spectral response of an eight-channel filter bank with a target channel spacing of 150 GHz. The actual average channel spacing is of 158 GHz with better than -30 dB crosstalk between adjacent channels.

The symmetry of the second-order filter suggests that no frequency mismatch should exist between the two microring resonators forming the filter since electron-exposure proximity effects and coupling-induced frequency shifts should affect both resonators similarly. However, a repeatable resonant frequency mismatch between the two resonators forming the filter was observed. By writing the filter at several different locations in the 100 um SEBL field, we observed that the frequency mismatch was a function of location. Hence, it is most probably due to intrafield distortions or digital-to-analog converter errors in the SEBL system. This frequency mismatch, once known, can be corrected using dose modulation by writing the two rings in the same filter with slightly different dose.

Based on the calibration experiments, the changes in exposure dose and ring radius needed to produce eight-channel filter banks with channel spacing ranging from 90 to 180 GHz were calculated and input to the SEBL layout. The filters were spaced by 100 um and all positioned identically in their respective SEBL field. The frequency mismatch due to intrafield distortion at this location was measured at calibration to be 8 GHz. To correct for this mismatch the average waveguide width of the lower ring in the second-order filters was narrowed by 0.24 nm by reducing its exposure dose by 0.7%. The fabrication process was similar to the one described.

Transmission measurements were taken for the common thru port of the filter banks and the individual drop port of each filter. Fig. 16 shows the transmission spectrum of a fabricated filter bank. The drop loss was found to be 1.5±0.5 dB. The resonant frequency of the microring filters was found to be controlled within the statistical error of the calibration experiment. The actual channel spacing of the fabricated filters was 4%–5% larger than the targeted spacing. This offset is due to a difference of 0.8 GHz/nm between the resonance frequency dependence on specified radius at calibration and what is seen in the filter banks. This is within the error of the calibration experiment, which is calculated to be 1.0 GHz/nm, for the resonance frequency dependence on specified radius. The calibration of the resonant frequency dependence on dose was found to be even more accurate. The average ring waveguide width change due to dose is measured to be 0.34 nm per 1% change in dose in the filter banks compared to 0.35 nm measured at calibration. This means that the change in average ring waveguide width per percent exposure dose increase varied by only 10 pm between the calibration experiment and the filter bank fabrication.

The effect of stochastic process variations on the frequencies of individual microrings was also investigated. It was found that the average ring-waveguide width stochastically varied with a standard deviation of 0.12 nm. A detailed discussion of these filter banks is presented in Ref. 10.

6. CONCLUSION

We have quantified the achievable relative dimensional control on nearby structures to be of the order of 0.1 nm. This is significantly better than the achievable absolute dimensional control, which is of the order of a few nanometers. This high relative dimensional control enables schemes such as multistage filters, integrated polarization diversity, and filter

banks with accurate frequency spacing. The first demonstration of multistage filters resulted in a through-port extinction of at least 51 dB, by far the highest reported in a microring filter. The first demonstration of polarization diversity showed almost complete elimination of polarization sensitivity, a first in strong confinement microphotonic devices.

REFERENCES

[1] M.A. Popović, M.R. Watts, T. Barwicz, P.T. Rakich, L. Socci, E.P. Ippen, F.X. Kärtner and H.I. Smith, "High-index-contrast, wide-FSR microring-resonator filter design and realization with frequency-shift compensation," Optical Fiber Comm. Conf., OFK1 (Optical Society of America, Washington, DC, 2005).

[2] Mitsubishi Rayon America Inc. (2004), aquaSAVE Datasheet, http://www.mrany.com

[3] M.A. Popović, C. Manolatou and M.R. Watts, "Coupling-induced resonance frequency shifts in coupled dielectric multi-cavity filters", Opt. Express **14**, 1208-1222 (2006).

[4] T. Barwicz, M.A. Popović, M.R. Watts, P.T. Rakich, E.P. Ippen and H.I. Smith, "Fabrication of Add-Drop Filters Based on Frequency-Matched Microring Resonators," J. Lightwave Technol. **24** (5), 2207-2218 (2006).

[5] M.A. Popović, T. Barwicz, M.R. Watts, P.T. Rakich, L. Socci, E.P. Ippen, F.X. Kärtner and H.I. Smith, "Multistage high-order microring-resonator add-drop filters," Opt. Lett. **31 (**17), 2571-2573, (2006).

[6] M.R. Watts, H.A. Haus, and E.P. Ippen, "Integrated mode-evolution-based polarization splitter," Opt. Lett. **30** (9), 967-969 (2005).

[7] M.R. Watts and H.A. Haus, Integrated mode-evolution-based polarization rotators, Opt. Lett. **30** (2), 138-140 (2005).

[8] T. Barwicz, M.R. Watts, M.A. Popović, P.T. Rakich, L. Socci, F.X. Kärtner, E.P. Ippen and H.I. Smith, "Polarization-transparent microphotonic devices in the strong confinement limit," Nat. Photon. **1**, 57-60 (2007).

[9] W. Holzwarth, T. Barwicz, M.A. Popović, P.T. Rakich, E.P. Ippen, F.X. Kärtner, and Henry I. Smith, "Accurate resonant frequency spacing of microring filters without postfabrication trimming," J. Vac. Sci. Technol. **B 24** (6), 3244-3247 (2006).

[10] F.X. Kärtner, S. Akiyama, G. Barbastathis, T. Barwicz, H. Byun, D.T. Danielson, F. Gan, F. Grawert, C.W. Holzwarth, J.L. Hoyt, E.P. Ippen, M. Kim, L.C. Kimerling, J. Liu, J. Michel, O.O. Olubuyide, J.S. Orcutt, M. Park, M. Perrott, M.A. Popović, P.T. Rakich, R.J. Ram, H.I. Smith and M.R. Watts, "Electronic photonic integrated circuits for high speed, high resolution, analog to digital conversion (Invited)," SPIE Proc. **6125**, 612503, (2006).